Finite-Volume Solutions to the Euler Equations in Transonic Flow

Wolfgang Schmidt*
Dornier GmbH, Friedrichshafen, Federal Republic of Germany
Antony Jameson†
Princeton University, Princeton, New Jersey
and
David Whitfield‡
Mississippi State University, Mississippi State, Mississippi

An efficient numerical method for the solution of the two- and three-dimensional transonic Euler equations has been used to compute the flow over airfoils, wings, and wing-body combinations. For two-dimensional flow, the Euler equation code has been coupled with an inverse boundary-layer integral method to compute viscous flow over transonic airfoils with shocks. All Euler methods are using the same mesh systems (O or C type) as well-established full-potential codes which can optionally also provide initial solutions. This allows for detailed comparisons with the full-potential solutions. Results are discussed in detail for lifting and nonlifting airfoils as well as the DFVLR-F4 transonic transport configuration.

I. Introduction

WHILE potential flow solutions have proved extremely useful for predicting transonic two- and three-dimensional flows with shocks of moderate strength, (e.g., see Refs. 1-3) typical of cruising flight of transport and some class of fighter aircraft, the approximation of ignoring entropy changes and vorticity production cannot be expected to give acceptable accuracy when the flight speed is increased into the upper transonic range. However, more important than the change in pressure rise across a shock as pointed out by Lock[4] are the effects on lifting flows due to the assumptions inherent to the Kutta condition in potential flow theory. One part of this paper will study this effect in detail.

Methods available for simulating transonic viscous flow over airfoils are either Navier-Stokes methods, e.g., Ref. 5, or inviscid methods coupled with boundary-layer solutions. Whereas the Navier-Stokes equations properly describe interacting flows, these equations are currently restricted from routine use because of computer requirements and lack in physical understanding. Inviscid flow boundary-layer coupling methods on the other hand require less computer resources, but have been developed only for irrotational inviscid flows and usually attached boundary layers, see Refs. 4, 6, and 7. In the present paper the Euler equation solver allowing for rotational inviscid flow is coupled with an inverse integral boundary-layer method to allow for attached or separated boundary layers, thus avoiding problems in dealing with strong shocks as reported by Lock.[4]

The third part of the paper deals with three-dimensional wing and wing-body flow. At present, only potential flow solvers based on either the small disturbance or full-potential solution are in use. Reference 8 presents an interesting review comparing different methods with experimental data. However, all methods exhibit the need for an added vortex sheet as discontinuity surface. Since the introduced jumps in potential are confined to be constant along $y=\text{const}$ lines rather than streamlines, those methods are physically incorrect near the wing tip or for small aspect ratio wings. These problems can be overcome by solving the full Euler equations in conservation form since they can capture discontinuities without explicitly introducing vortex sheets.

Based on previous experiences on airfoil, inlet, and wing computations the finite-volume approach as introduced by MacCormack[9] has been chosen. Recent efforts, however, to improve the efficiency have led to a new multistage, two-level scheme which is described in detail in another paper of the 1981 AIAA-FPD conference.[10] The Euler codes based on these schemes operate on O or C meshes provided by existing full-potential solvers. Since the same mesh is being used, this allows for direct comparisons between full potential and Euler solution, moreover, the full-potential solution can be used as starting solution for the Euler solver.

At present the methods have been applied to lifting and nonlifting airfoils, cascades, wings, wing-body combinations, and inlets. In the present paper detailed comparisons are given for lifting and nonlifting airfoils as well as the DFVLR-F4 wing-body combination which is a standard test case in GARTEur AG01. Special attention is given to the effect of separation in inviscid compressible flow as studied on the circular cylinder. This phenomenon was apparently first noted by Salas.[16] Most cases have been run on an IBM 3031; the codes, however, have also been tested on CDC 6600, CYBER 203, and CRAY 1 machines.

II. Euler Equation Method

The numerical method used to solve the time-dependent Euler equations is described in detail in Ref. 10. The version used for all cases discussed in the present paper is the unsplit four-stage two-level scheme with the enthalpy-forcing term and the local time stepping. A blend of second and fourth differences is used to construct dissipative terms of a filter-type.

The far field boundary conditions are nonreflecting and allow either for sub- or supersonic freestream Mach numbers. All solid surfaces have no flux boundary conditions, the wall pressure being extrapolated from the field. For viscous simulations the flux through the wall is given by the source velocity equivalent to the boundary-layer displacement thickness.

Presented as Paper 81-1265 at the AIAA 14th Fluid and Plasma Dynamics Conference, Palo Alto, Calif., June 23-25, 1981; submitted July 20, 1981; revision received April 29, 1982.

*Head, Aerodynamics Department. Associate Fellow AIAA.
†Professor, Department of Mechanical and Aerospace Engineering.
‡Professor, Department of Aerospace Engineering. Member AIAA.

III. Inverse Boundary-Layer Method

The singularity associated with boundary-layer computations at separation is avoided by using an inverse boundary-layer method. By specifying, for example, the displacement thickness distribution instead of the pressure distribution (a so-called inverse method) this singularity is removed[11] and boundary-layer computations can proceed through separated regions. The inverse method used here is the mean-flow kinetic energy integral method described in Ref. 12. This method is based on turbulent boundary-layer velocity profiles that describe separated or attached flow. The same calculation scheme is used whether the flow is attached or separated and hence no switching or artificial fix is required for points near separation. The dissipation integral is evaluated at each streamwise location using the velocity profiles and the Cebeci-Smith algebraic eddy viscosity model.

In an inverse boundary-layer method, pressure is a dependent variable, and in the particular inverse method used here the displacement thickness (δ^*) distribution is specified. The method used to provide a rational, a priori, specification of the δ^* distribution is the method of Carter.[13] Carter's method can be written as

$$\delta^{*(m+1)} = \delta^{*(m)} + \omega\delta^{*(m)}\,(u_{e,v}/|q|_{w,i} - 1) \qquad (1)$$

where $\delta^{*(m+1)}$ is the new displacement thickness at a streamwise location; $\delta^{*(m)}$ is the displacement thickness from the previous iteration; $u_{e,v}$ is the local velocity at the edge of the boundary layer obtained from the last boundary-layer solution; $|q|_{w,i}$ is the magnitude of the local velocity vector obtained from the last Euler equation solution; and ω is the relaxation parameter.

IV. Viscid-Inviscid Coupling

The method used to achieve viscid-inviscid coupling is the surface source model (or the method of equivalent sources of Lighthill[14]). This method has an advantage over the effective displacement surface approach in that a surface source mass flux is imposed as a boundary condition in the inviscid calculation at the physical body surface or in the wake, and hence mesh adjustment during the iteration process is not required. The surface source mass flux, $(\rho v)_n$, imposed at the physical surface is given by

$$(\rho v)_n = \frac{\mathrm{d}(\rho_e u_e \delta^*)}{\mathrm{d}x} \qquad (2)$$

where $(\rho v)_n$ is the local mass flux normal to the surface. The right-hand side of Eq. (2) is evaluated after each inverse boundary-layer solution to determine $(\rho v)_n$ for subsequent inviscid calculations.

The viscid-inviscid interaction calculation scheme proceeds in the following steps.

1) The Euler equation solution is advanced 20-50 cycles with $(\rho v)_n \equiv 0$.

2) An inverse boundary-layer solution is obtained with $\delta^{*(1)}$ given by Eq. (1), where $\delta^{*(0)}$ is a flat plate distribution, $u_{e,v}$ is constant at the freestream value (u_∞), and $|q|_{w,i}$ is obtained from the last cycle of the Euler equation solution.

3) The Euler equation solution is advanced 20-50 cycles with $(\rho v)_n$ held fixed at the value given by Eq. (2).

4) An inverse boundary-layer solution is obtained with $\delta^{*(m+1)}$ given by Eq. (1).

5) Steps 3 and 4 are repeated until convergence on δ^* or c_p (surface pressure coefficient) is obtained.

The number of cycles the Euler equation solution is advanced in steps 1 and 3 depends upon the problem. For example, if strong shocks form in the early cycles of the Euler equation solution and if over-relaxation is used, like $\omega = 2$, it can be advantageous to call the inverse boundary-layer solution after only a few cycles. It is possible to obtain a converged viscid-inviscid interaction solution in fewer cycles than required to obtain a converged inviscid solution due to a weaker shock resulting from the inclusion of viscous effects. However, all solutions presented were cycled from 1.5 to 2 times, the same number of cycles required for a purely inviscid solution.

V. Mesh Generation

Two- and three-dimensional contour-conformal grids are constructed using standard O- or C-type procedures. Since the mesh generation has been separated from the Euler solver, any mesh can be used, as long as the O or C logics are not violated, because they will influence the lines or surfaces where boundary conditions have to be provided. In the present paper parabolic coordinates are used as C-type mesh and a mapping to a near circle as O-type mesh. For three-dimensional wings parabolic coordinates are used in constant spanwise stations while for arbitrary wing-body combinations a Thompson-type mesh generator has been adapted based on the concept of Yu.[15]

Standard meshes for two-dimensional studies have been 128×32 for the O-type and 121×30 for the C-type. Special attention has been given to the O-type mesh since it allows for a very dense spacing at the trailing edge, thus allowing studies of the trailing-edge behavior. For viscous flows, however, the C-type mesh seems to be favorable since it allows for a dense spacing of the wake region. The mesh near the trailing edge and in the wake can easily be aligned with the wake-streamline, which will provide a good capturing of the possible discontinuity in tangential velocity.

Standard meshes for three-dimensional studies up to now have been restricted to $40 \times 8 \times 8$ and $80 \times 16 \times 16$, since the whole computation is being done in core.

Mesh refinement techniques can easily be adapted, but, however, have not been used in the present study because of the use of full-potential methods to provide starting solutions.

VI. Kutta Condition

In two-dimensional lifting inviscid isentropic flows a Kutta condition has to be specified at the trailing edge which generally is implemented in computational methods by requiring the static pressure to be equal at both the upper and lower surface trailing edge. Since in potential flow, total pressure is constant everywhere, this condition will force the total velocity on both sides to be zero for non-zero trailing-edge angle and equal and finite for zero trailing-edge angle.

In rotational flow, e.g., transonic flow with a shock on the upper surface, the total pressure behind the shock on the upper surface is smaller than on the lower surface corresponding point, thus forcing a difference in the speed for continuous static pressure. This forces the inviscid flow to leave at the trailing edge and to be single valued since no solution with $|q| \neq 0$ on both the upper or lower surface is possible. The only possible solution is the one depicted on Fig. 1 where the flow will leave tangent to the surface with the higher total pressure smoothly and form a slip line. In compressible flows without shocks, again, only the one solution with $|q| = 0$ at the trailing edge and a flow leaving in the bisector direction is possible. This is due to the fact that any flow around the trailing edge would cause expansion to $M \to \infty$ which has to be terminated by a shock if the flow will leave the upper surface (Fig. 1). Again, this would cause two different tangential velocities at both sides of the fictitious Kutta point which is impossible.

To study these effects for smooth, round trailing edges, some numerical experiments have been performed on the circular cylinder test cases initiated by Salas[16] who found similar results. The results shown in Figs. 2 and 3 have been achieved in a 64×32 0-mesh for a half-cylinder.

Figure 2 portrays nicely the results for $M_\infty = 0.20$ in pressure distribution solving the full-potential equation and the Euler equations. Both solutions are fully converged to a

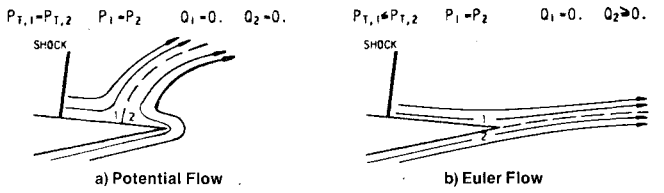

Fig. 1 Trailing-edge flow and Kutta condition in lifting airfoil flow.

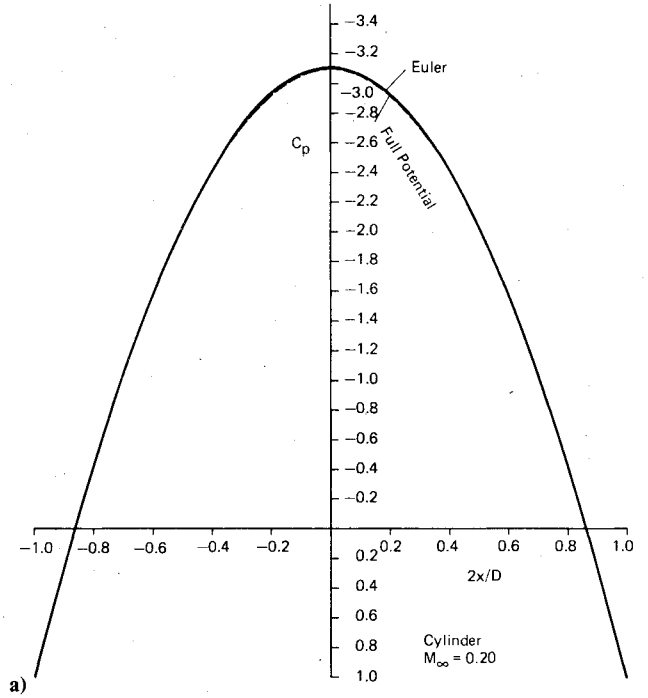

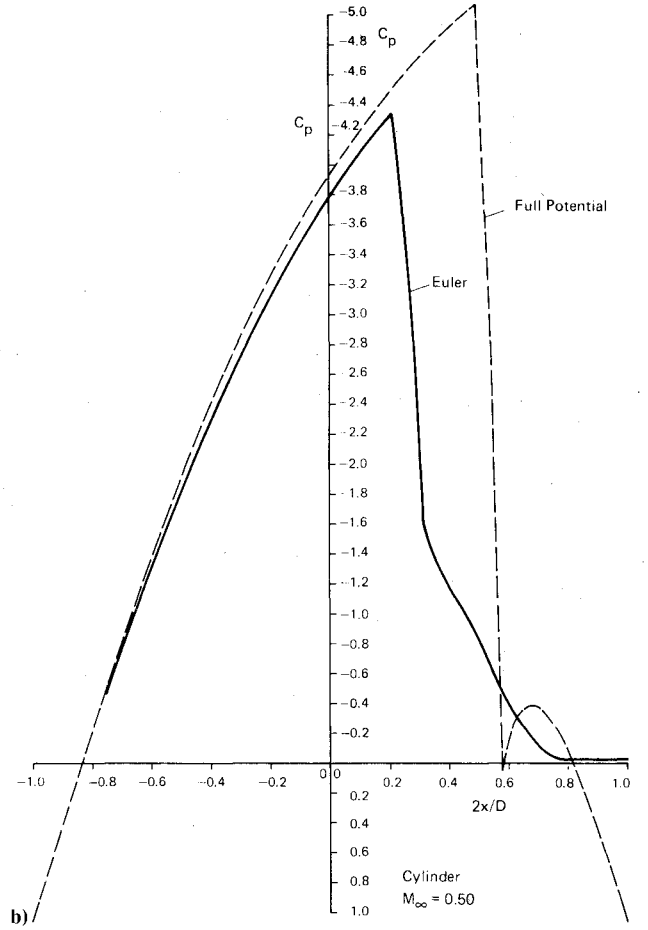

Fig. 2 Circular cylinder flow at $M_\infty = 0.20$ and 0.50, c_p distribution as full-potential and Euler solution.

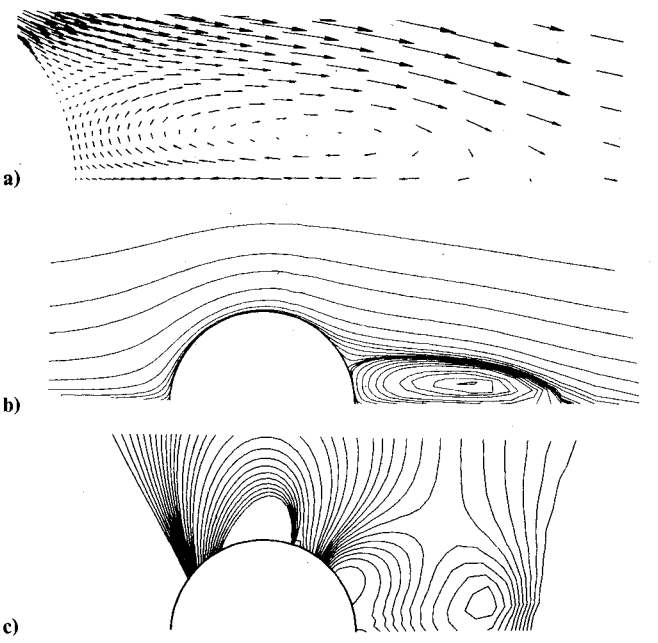

Fig. 3 Velocity vector plot and isobar plot for the Euler solution of the circular cylinder flow at $M_\infty = 0.50$. a) Velocity vectors, b) streamlines, and c) isobars.

residual of 10^{-12} and both agree completely. For $M_\infty = 0.50$, Fig. 2 shows quite different results. The highly converged full-potential solution gives a very strong shock and stagnation is reached with the correct static pressure and $q = 0$ at the rear stagnation point. The Euler solution indicates only minor differences at the forward part of the cylinder; however, shock position as well as pressure ahead and behind the shock differ quite a lot from the full-potential solution. Most surprisingly, starting from $2x/D \sim 0.78$ the static pressure from the Euler solution is constant and almost equal to $c_p = 0$. Figure 3 clarifies the results by presenting the direction of the local velocity vectors. The flow separates from the smooth surfaces and forms a recirculating "dead-air" region with very small velocities ($q \leq 0.01 U_\infty$). It is interesting that the well-known phenomena of nearly constant pressure in such a dead-air region is computed by the present method without specifying anything specifically about this region. Although inviscid separation sounds strange at first, it can be proven to be correct. The reason for this separation is the total pressure loss and the vorticity due to the shock, rather than due to the boundary layer. However, the consequences are similar since the flow due to the total pressure loss at the wall streamline does not have enough kinetic energy to stagnate at the rear stagnation point. It should be noted that this inviscid separation point can be found to be always behind the one known from viscous flow analysis. It can arise as a limit for $Re \to \infty$ in compressible flow if the total pressure losses are significant or the onset flow is rotational.

Since these examples indicate the basic capabilities of inviscid flow computations with the full Euler equations, the treatment of wakes in three-dimensional flow will only be mentioned briefly. All Kutta conditions pertinent to the problem in consideration will show up automatically. Since the method is written in full conservation form, discontinuities like shocks and slip lines are also captured properly. As known from supersonic flow studies, the accuracy can be improved by mesh alignment, which recommends the use of a C-type mesh for wings since this will allow easily for wake alignment.

VII. Results

The efficiency and accuracy of the Euler solver has been confirmed by numerical experiments. Some typical results are presented here. Nonlifting results are shown in Ref. 10 for the

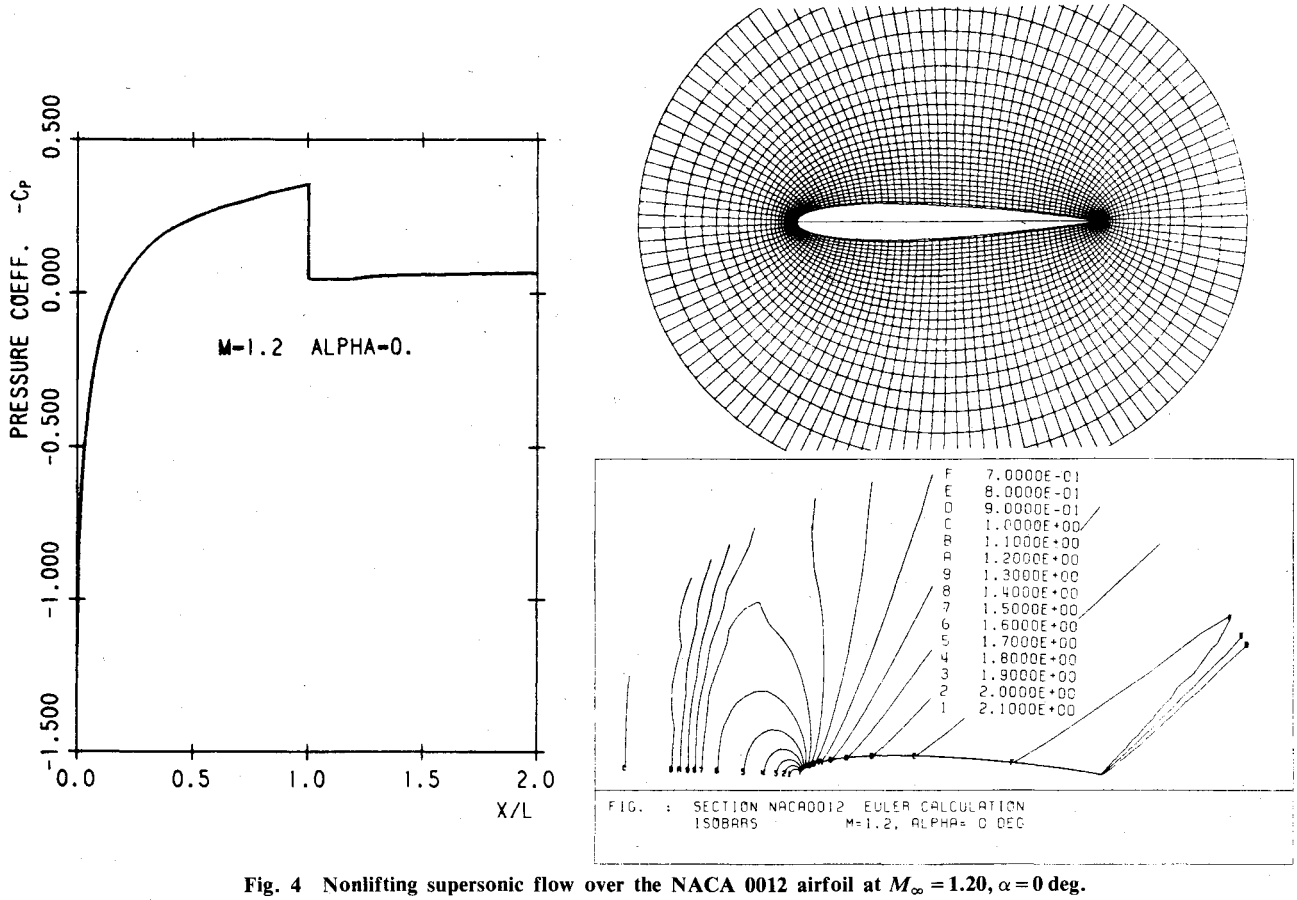

Fig. 4 Nonlifting supersonic flow over the NACA 0012 airfoil at $M_\infty = 1.20$, $\alpha = 0$ deg.

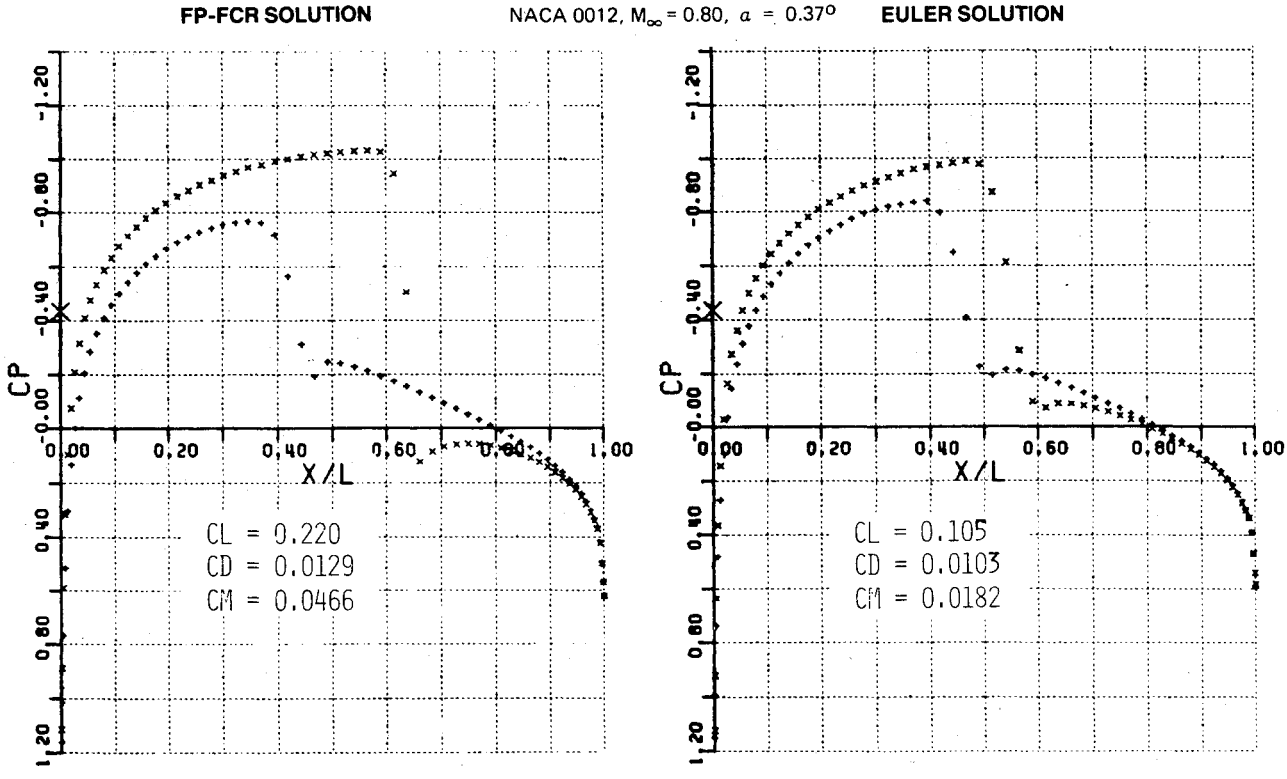

Fig. 5 Lifting transonic flow over the NACA 0012 airfoil at $M_\infty = 0.80$, $\alpha = 0.37$ deg. Comparison between Euler and full-potential solution.

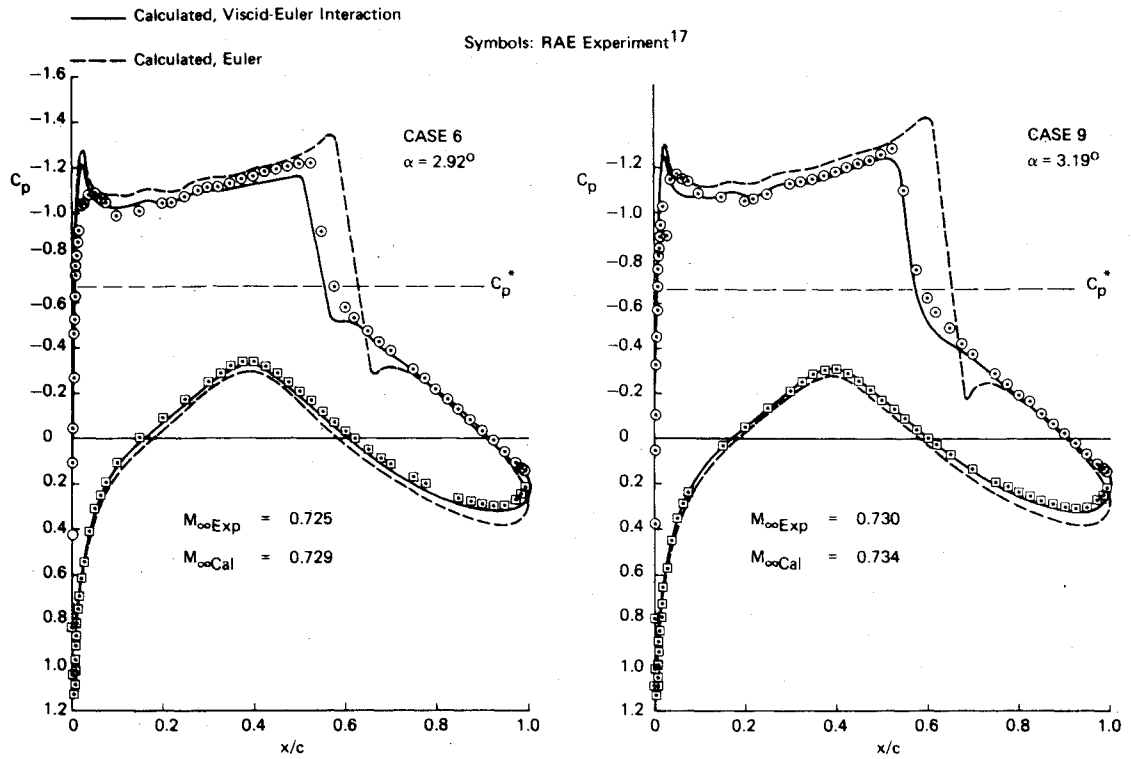

Fig. 6 Surface pressure distributions on the RAE 2822 airfoil. Comparisons with experiments[17] (cases 6 and 9).

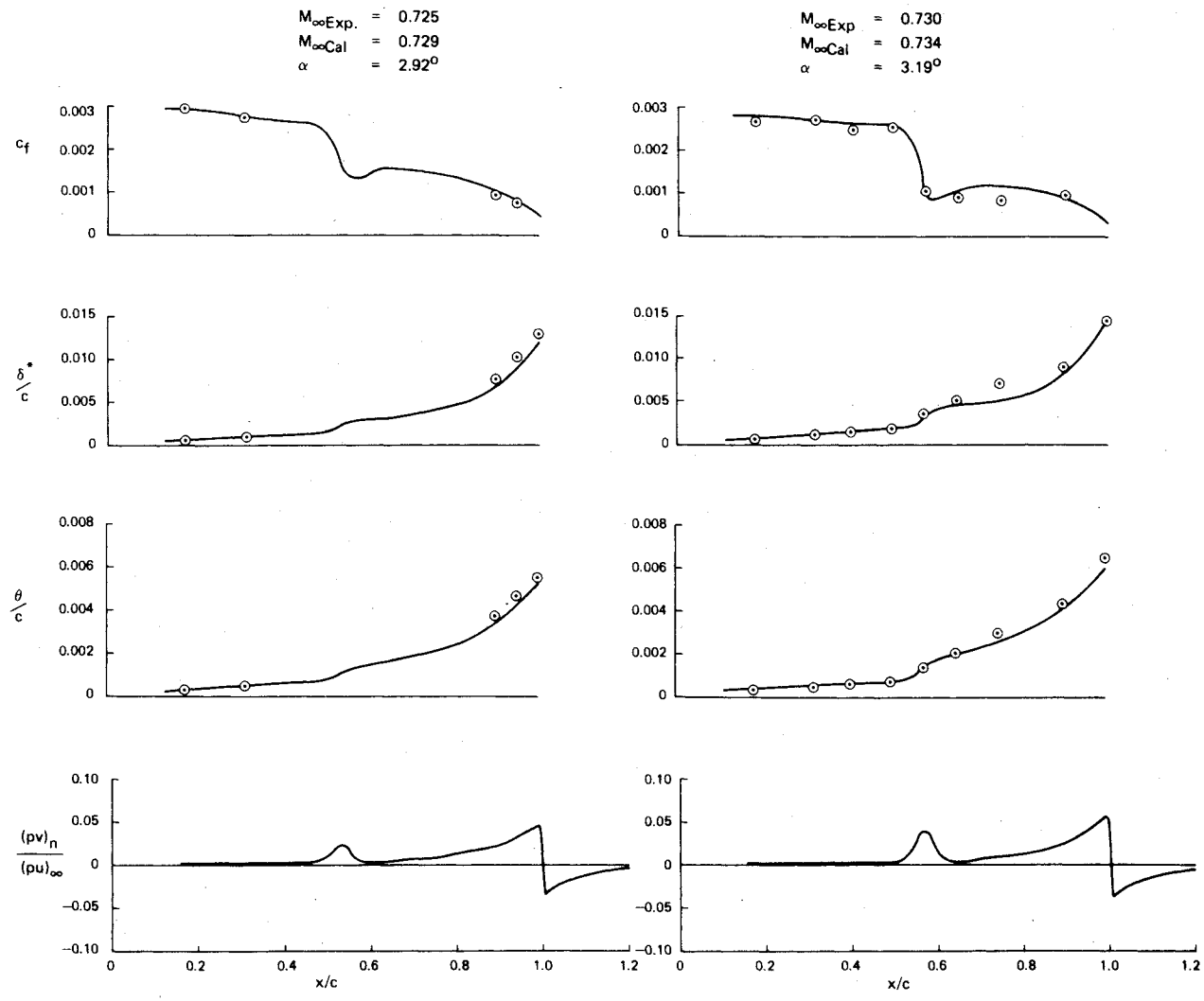

Fig. 7 Comparison of computed boundary-layer data for the RA 2822 airfoil and experiments[17] (cases 6 and 9).

NACA 0012 airfoil. In a 64×32 0-mesh for the half-plane the highly converged full-potential solution using multi-grid and the Euler solution show 8% chord difference in shock position, the pressure jump is smaller, as expected from the Rankine-Hugonoit condition, and the trailing-edge pressure is reduced owing to the total pressure loss. Figure 4 shows corresponding results for a supersonic freestream Mach number, demonstrating the flexibility of the present method.

Figure 5 portrays the comparison for lifting flow over the NACA 0012 airfoil using a 128×32 0-mesh. Again, the full-potential MAD solution has been used as starting solution for the Euler solver. The converged solution was reached after 500 Euler cycles with stability condition CFL = 2.8. This time, not only are their differences in the shock strength and position significant, but also in the complete pressure distribution. Lift, drag, and moment coefficients are quite different. Again, trailing-edge pressure is slightly reduced. The difference in lift can be explained as an effect coming from the trailing-edge Euler solution which does not need any explicit Kutta condition. Since there exists a total pressure loss on the upper surface, the flow is leaving the lower surface smoothly, which corresponds to a small flap deflected upwards in potential flow.

The experimental data of Cook, McDonald, and Firmin[17] include surface pressure and boundary-layer information for transonic flow about the RAE 2822 airfoil. Two sets of experimental data, denoted as cases 6 and 9 in Ref. 17, are considered. Unfortunately these data, like all available transonic airfoil data, are not interference-free.

In the present computations only the nominal Mach number of the wind tunnel results has been corrected by $\Delta M = 0.004$ for both cases. The Reynolds number based on chord was $Re = 6.5 \times 10^6$. No adjustments have been made to match lift. The solutions were all obtained in a C-type mesh with 128×30 volumes. Both the interaction solutions and the inviscid solutions were run 1000 cycles in the Euler code. For

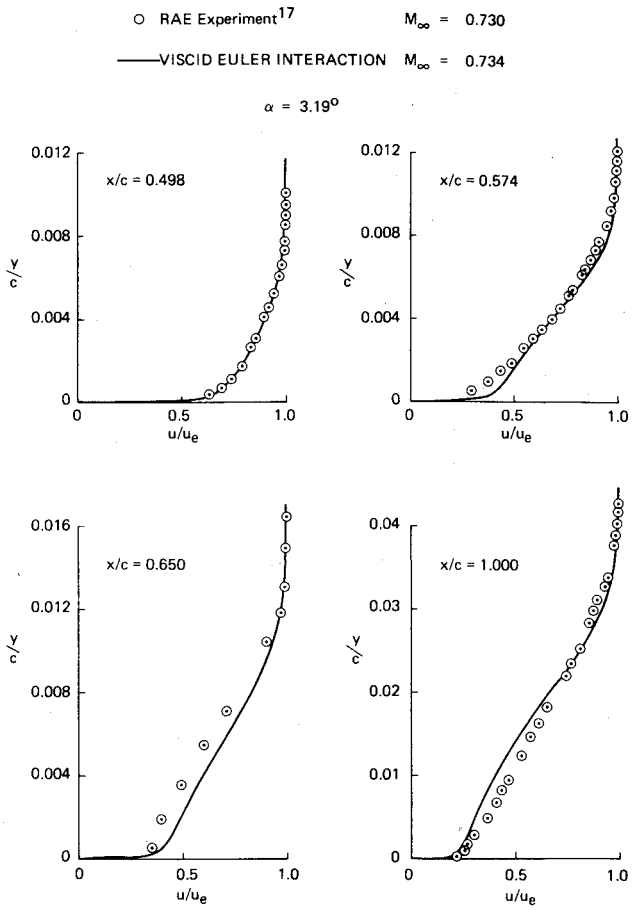

Fig. 8 Comparison of computed boundary-layer velocity profiles for the RAE 2822 airfoil with experiments[17] (case 9).

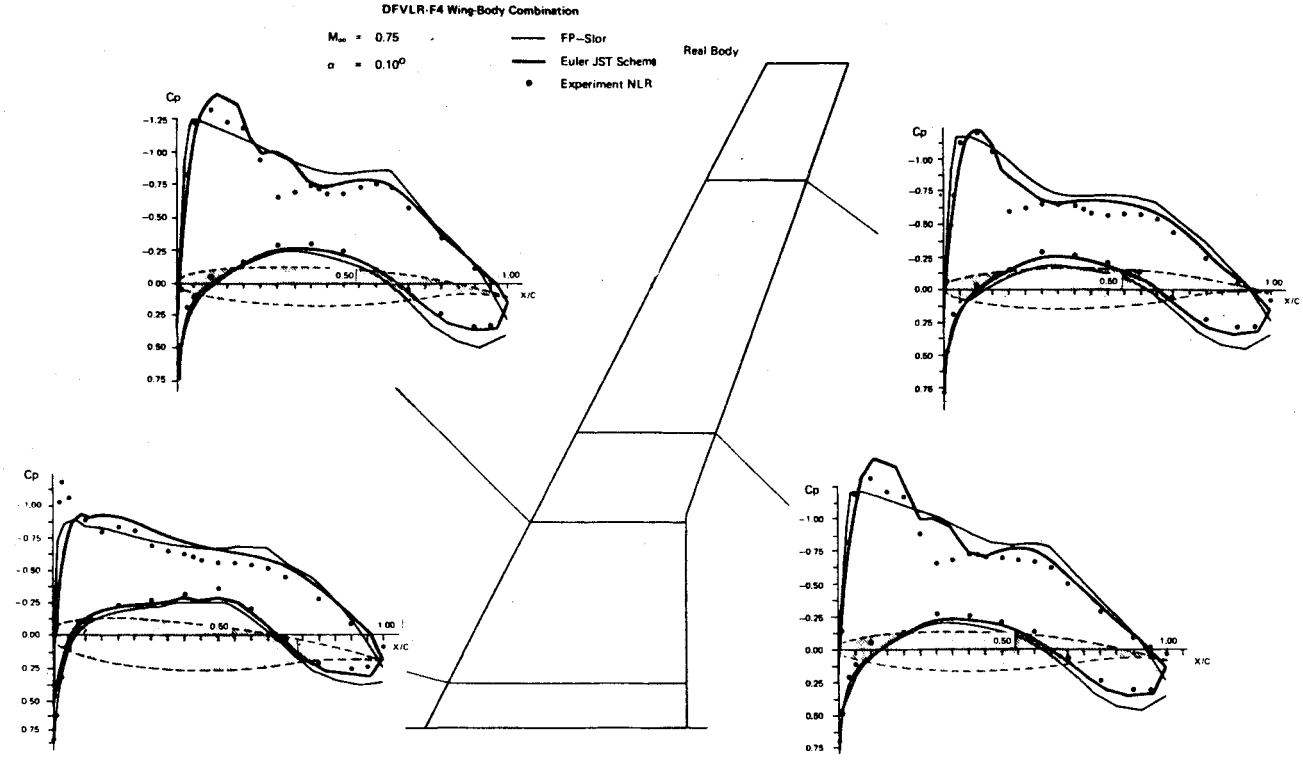

Fig. 9 Comparison of three-dimensional Euler and full-potential solutions with experiment[18] for the transport configuration DFVLR-F4 wing plus real fuselage.

the viscous cases the boundary-layer method was called every 50 cycles.

Comparisons of calculated and measured surface pressure data are given in Fig. 6. The agreement with the experimental data is quite good, even for the trailing-edge region. The difference in shock position for case 6 is within the uncertainties in Mach number corrections.

Comparisons of calculated and measured boundary-layer data are given in Fig. 7. The calculated boundary-layer displacement thickness (δ^*/c) and momentum thickness (θ/c) distributions are slightly below the experimental data over the aft portion of the airfoil for case 6. However, the calculated shock location is slightly forward of the experimental shock location as mentioned above, which may contribute to this difference. The calculated c_f, δ^*/c, and θ/c distributions for case 9 with the stronger shock are in fairly good agreement with the experimental data, even in the shock-boundary-layer interaction region. A more detailed comparison of calculated and measured data throughout the shock region and at the trailing edge is given in Fig. 8 by boundary-layer velocity profile comparisons. The agreement between calculated and measured data is considered good. Calculated distributions of the source velocity $(\rho v)_n$ are included in Fig. 7. This term becomes significant in, and downstream of, the shock with large positive values occurring in the shock region and at the trailing edge. The source velocity becomes negative in the wake and reaches a minimum just aft of the trailing edge.

Finally, the capabilities of the present Euler method to solve the inviscid three-dimensional transonic or supersonic flow over wings and wing-body combinations are shown in Fig. 9 for the DFVLR-F4 wing-body transport configuration. This configuration represents a Transonic Action Group wing design and was chosen to be a standard test case within the European GARTEur AG01. Since the three-dimensional wing-body code is operating fully in core, we are presently limited on the IBM 3031 to $80\times16\times16$ volumes. The Euler solution was obtained using a finite-volume full-potential (FPE) SLOR solution in the same mesh as the initial solution. The FPE-solution was converged up to a residual of 10^{-4}. The Euler solution did converge after 300 cycles with CFL = 2.8, and further 800 cycles did not change the solution any more. It is interesting to note that in the same mesh the Euler solution can resolve details better since velocities and pressures are direct variables while in the potential solution the velocities and ergo pressure result from numerical differentiation. In comparison with the experimental data, both the FPE and the Euler solution seem to need a correction in Mach number to match the experimental data on the lower surface. The upper surface, however, is in much better agreement for the Euler solution and would even improve owing to the expected Mach number correction. The differences have not been explored completely yet, but they seem to be mainly due to the better Kutta and wake treatment in the Euler solution.

VIII. Conclusions

The objectives of the present paper were to develop an efficient and accurate Euler solver to compute transonic and supersonic flow over two- and three-dimensional configurations. Since the same meshes were used in the Euler solver as for well-established finite-volume full-potential solvers, the main differences between Euler and fully conservative FPE solutions could be demonstrated. The most important information has been that Euler solvers do not need any explicit Kutta condition to be unique in either two- or three-dimensional flow. Even on smooth surfaces separation can occur in inviscid compressible flow caused by total pressure loss and vorticity due to a shock. These effects help explain the a priori unexpected differences between lifting Euler and full-potential solutions. For viscous flow the Euler equations solver has been successfully coupled with an inverse boundary-layer method. In comparison with experimental data, the wind tunnel corrections in Mach number and angle of attack as suggested by users of full-potential solvers[4,6] do not result in total agreement if the Euler equations are being solved. High quality interference free experimental data are needed to verify methods like the present one in detail. Unfortunately such data are evidently not available.

Computer times of the present Euler solver are 1 ms/vol. and cycle on the IBM 4341 computer. Corresponding times on the CRAY-1 computer are 0.01 ms. The CYBER 203 requires more than twice that time.

Acknowledgment

This work was partially supported by the Ministries of Defense and of Research and Technology of the Federal Republic of Germany.

References

[1] Jameson, A. and Caughey, D.A., "A Finite Volume Method for Transonic Potential Flow Calculations," AIAA Paper 77-635, 1977.

[2] Boppe, C.W., "Towards Complete Configurations Using an Embedded Grid Approach," NASA-CR 3030, July 1980.

[3] Schmidt, W., "Aerodynamic Subsonic/Transonic Aircraft Design Studies by Numerical Methods," AGARD CP 285, Paper 9, 1980.

[4] Lock, R.L., "A Review of Methods for Predicting Viscous Effects on Aerofoils and Wings at Transonic Speeds," AGARD-CPP-291, 1980.

[5] Deiwert, G.S., "Recent Computation of Viscous Effects in Transonic Flow," *Lecture Notes in Physics,* No. 56, Springer, Berlin, 1976, pp. 159-164.

[6] Melnik, R.E., "Turbulent Interactions on Airfoils at Transonic Speeds—Recent Developments," AGARD-CPP-291, 1980.

[7] Longo, J., Jameson, A., and Schmidt, W., "DOFOIL-A Viscous Analysis Program for Transonic Airfoil Flow," Dornier FB 81, May 1981.

[8] van der Kolk, J.Th. and Slooff, J.W., "A Comparison of Computational Results for Transonic Flow Around the ONERA-M6 Wing," NLR-REPORT, GARTEur, AG (AD) 01, 1981.

[9] Mac Cormack, R.W. and Warming, R.F., "Survey of Computational Methods for Three-Dimensional Supersonic Inviscid Flows with Shocks," in *Advances in Numerical Fluid Dynamics*, AGARD LS 64, 1973.

[10] Jameson, A., Schmidt, W., and Turkel, E., "Numerical Solutions of the Euler Equations by Finite Volume Methods Using Runge Kutta Time Stepping Schemes," AIAA Paper 81-1259, June 1981.

[11] Catherall, D. and Mangler, K.W., "The Integration of the Two-Dimensional Laminar Boundary Layer Equations Past the Point of Vanishing Skin Friction," *Journal of Fluid Mechanics*, Vol. 26, Part 1, 1966, pp. 163-183.

[12] Whitfield, D.L., Swafford, T.W., and Jacocks, J.L., "Calculation of Turbulent Boundary Layers with Separation, and Viscous-Inviscid Interaction," *AIAA Journal*, Vol. 19, Oct. 1981, pp. 1315-1322.

[13] Carter, J.E., "A New Boundary Layer Inviscid Iteration Technique for Separated Flow," AIAA Paper 79-1450, July 1979.

[14] Lighthill, M.J., "On Displacement Thickness," *Journal of Fluid Mechanics*, Vol. 4, Part 4, 1958, pp. 383-392.

[15] Yu, N.J., "Grid Generation and Transonic Flow Calculations for Three-Dimensional Configurations," AIAA Paper 80-1391, July 1980.

[16] Salas, M.D., "Rotationally Induced Inviscid Wake Bubble," Paper 10 presented at the AIAA 5th CFD Conference, 1981.

[17] Cook, P.H., McDonald, M.A., and Firmin, M.C.P., "Aerofoil RAE 2822 Pressure Distributions and Boundary Layer Measurements," AGARD-AR-138, 1979.

[18] Slooff, J.W., "F-14 Wing. Results of Pressure Measurements (NLR-Test) for the Theoretical Test Cases," NLR Note AT/2789, Oct. 1980.